

Experimental and numerical investigations into collapse behaviour of thin spherical shells under drop hammer impact

N.K. Gupta ^{a,*}, N. Mohamed Sheriff ^b, R. Velmurugan ^c

^a *Applied Mechanics Department, IIT Delhi, India*

^b *Mepco Schlenk Engineering College, Sivakasi, India*

^c *Aerospace Engineering Department, IIT Madras, Chennai, India*

Received 20 September 2005; received in revised form 4 August 2006

Available online 20 September 2006

Abstract

A study of the collapse behaviour of hemi spherical and shallow spherical shells and their modes of deformation under impact loading are presented in this paper. Aluminium spherical shells of various radii and thicknesses were made by spinning. These were subjected to impact loading under a drop hammer and the load histories were obtained in all the cases. Three-dimensional numerical simulations were carried out for all the tested specimen geometries using LS-DYNA[®]. Material, geometric and contact nonlinearities were incorporated in the analysis. The uni-axial stress–strain curve for the material was obtained experimentally and was assumed to be piecewise linear in the plastic region. The results from impact experiments are used for the validation of the numerical simulations. Three distinct modes of deformation, namely local flattening, inward dimpling and formation of multiple numbers of lobes were analysed and influence of various parameters on these modes is discussed.

© 2006 Elsevier Ltd. All rights reserved.

Keywords: Spherical shells; Dimpling; Buckling; Axial load; Energy absorption; Impact; Lobes

1. Introduction

Experiments (Kitching et al., 1975; Gupta et al., 1999) have shown that the collapse of spherical shells between two flat platens is initiated with a local flattening over a short period of time, followed by inward dimpling and formation of integral number of lobes. Earlier studies on quasi-static compression of these shells (Updike, 1972; De'Oliveria and Wierzbicki, 1982; Kinkead et al., 1994) have analysed their collapse behaviour considering the inward dimpling as the main collapse mode. Equations developed for the computation of

* Corresponding author. Tel.: +91 11 2659 1178; fax: +91 11 2658 1119.

E-mail address: nkgupta@am.iitd.ernet.in (N.K. Gupta).

Nomenclature

t	average thickness in mm
σ_0	initial yield strength in MPa
σ_y	instantaneous yield strength in MPa
R	mean radius of the sphere in mm
H	specimen height (initial) in mm
E	elastic modulus in MPa
L	span of the shell in mm
M_s	striking mass in kg
ϵ_{eff}^p	effective plastic strain
β	hardening parameter
h	total compression of the shell at any stage of compression
r	mean radius of parallel circle of the shell at the contact with the plate
V_i	impact velocity of the drop mass
Z	depth of shells

mean collapse load in [Updike \(1972\)](#) and [De'Oliveria and Wierzbicki \(1982\)](#) are independent of the radius of the shell. Rolling and stationary plastic hinges were considered in [Gupta et al. \(1999\)](#) and a simplified analysis was presented for the axisymmetric inward dimpling as well as non-axisymmetric deformation leading to the formation of integral number of lobes.

It is seen that relatively thick shells deform axisymmetrically and a simplified two-dimensional numerical simulation is sufficient to study this phenomenon. Such shells were studied experimentally and numerically by [Gupta and Venkatesh \(Gupta and Venkatesh, 2004\)](#). They employed the finite element code FORGE 2 and considered local flattening and inward dimpling. However studies on three-dimensional simulations which are of help in understanding the phenomenon associated with all the collapse modes including non-axisymmetric deformation, and transitions therein, are not available.

In this paper, we present numerical and experimental studies carried out to analyse the collapse behaviour of spherical shells of different radii, height and thicknesses, under impact loading. The radius to wall thickness ratios (R/t) of these shells were varied between 28 and 219. All tests were repeated up to five times and those with results within 3% were taken for the analysis. The buckling and post buckling behaviour of spherical shells were simulated using an explicit software code LS-DYNA. Nonlinearities of material, geometry and contact are included in the analysis. The analysis presented is three-dimensional and thus all the stages of deformation viz local flattening, inward dimpling and formation of non-axisymmetric lobes in relatively thin shells have been simulated. Numerical results thus obtained compare well with the experiments. The results show that the mean collapse load varies with both the thickness as well as the radius of the shell.

Table 1
Metallurgical composition of specimen material

Comp.	t			
	0.70 mm	0.90 mm	1.20 mm	1.60 mm
Mg%	<0.50	<0.50	<0.50	<0.50
Si%	0.51	0.42	0.45	0.50
Cu%	0.10	0.10	0.11	0.10
Zn%	0.38	0.37	0.38	0.41
Mn%	0.02	0.02	0.08	0.11
Ti%	0.02	0.02	0.04	0.03
Cr%	0.04	0.04	0.04	0.04
Al	Bal	Bal	Bal	Bal

Table 2
Characteristic dimensions of spherical specimens tested

Specimen no.	Span L in mm	Radius R in mm	Depth H in mm	Mean thickness t in mm	R/t
H1	91	45	45.0	0.70	64.29
H2	90	45	45.2	0.90	50.00
H3	91	45	45.3	1.18	38.14
H4	90	45	45.2	1.60	28.13
H5	205	102	103.4	0.65	156.92
H6	206	102	103.8	0.89	114.60
H7	208	102	103.9	1.17	87.18
H8	307	153	154.4	0.70	218.57
H9	308	153	153.8	0.90	170.00
H10	306	153	153.5	1.18	129.66
H11	204	102	102.4	1.60	63.75
H12	307	153	153.2	1.58	96.84
S1	196	102	71.9	0.71	145.71
S2	196	102	72.4	0.89	114.61
S3	198	102	72.9	1.18	86.44
S4	297	153	105.4	0.70	218.57
S5	295	153	105.7	0.88	173.86
S6	297	153	105.3	1.18	129.16

Table 3
Typical thickness variation of tested specimens

Specimen	Locations							Mean thickness (mm)
	1	2	3	4	5	6	7	
H1	0.70	0.70	0.70	0.70	0.70	0.69	0.69	0.70
H6	0.90	0.90	0.90	0.89	0.89	0.89	0.88	0.89
H12	1.60	1.59	1.59	1.58	1.58	1.58	1.58	1.58
S3	1.20	1.20	1.18	1.18	1.18	1.17	1.17	1.18
S5	0.90	0.90	0.89	0.88	0.88	0.87	0.86	0.88

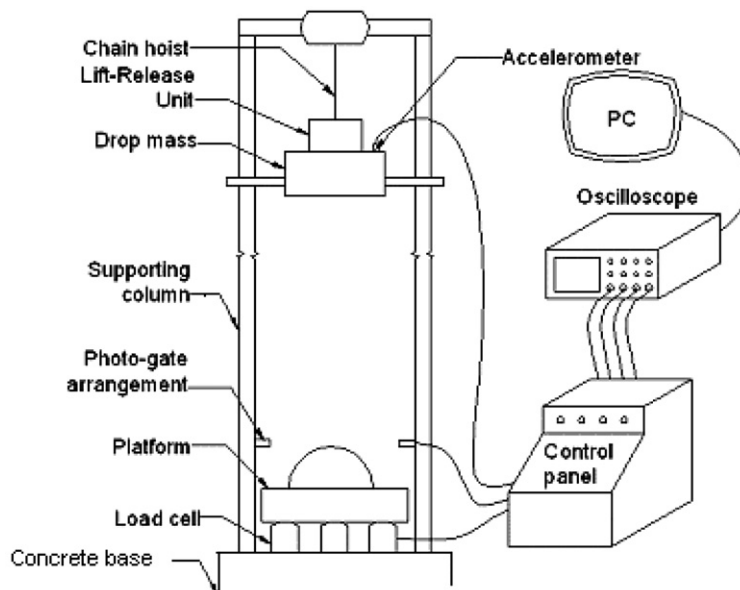


Fig. 1a. Drop mass setup – schematic diagram.

Table 4
Comparison of energy with numerical analysis and experiments

Specimen	Comp. in mm	Intended velocity in m/s	Drop height in mm	Measured velocity in m/s	Mass in kg	Average load in kN		Energy in J	
						Expt.	Num.	Expt.	Num.
H1	15.6	2.0	204	1.772	27	0.895	1.23	17.90	19.19
H2	19.4	2.0	204	1.879	37	3.200	3.64	62.08	70.62
H3	18.9	2.5	318	2.258	37	3.515	3.86	70.30	72.96
H4	16.8	2.75	385	2.658	37	6.731	7.34	114.62	123.31
H5	21.3	2.0	204	1.960	37	2.950	3.30	62.83	90.20
H6	20.4	2.0	204	1.920	37	3.200	3.96	65.28	80.78
H7	35.4	10.0	5097	9.980	27	13.420	14.90	475.12	565.25
H8	44.6	5.0	1274	4.846	27	2.489	3.90	117.01	173.40
H9	47.6	5.5	1542	5.425	27	5.653	5.82	265.67	277.03
H10	47.8	6.5	2153	6.264	27	8.545	9.70	401.59	463.66
H11	36.2	5.0	1274	4.970	27	8.270	8.960	299.38	324.35
H12	50.5	6.0	1835	5.930	27	9.160	10.42	459.83	526.21
S1	37.2	3.5	624	3.200	27	3.050	3.35	113.46	124.72
S2	29.4	3.0	459	2.980	27	3.870	4.22	113.78	124.07
S3	33.2	4.0	815	3.820	27	4.460	4.86	148.07	161.35
S4	61.62	4.0	815	3.930	27	3.200	3.48	197.20	214.43
S5	49.1	4.5	1032	4.150	27	4.18	4.55	205.24	223.41
S6	34.9	4.5	1032	4.200	27	6.25	7.27	218.13	253.72

2. Experiments

Spherical shells were made from commercially available aluminium sheets of thickness 0.7, 0.9, 1.2 and 1.6 mm by the process of spinning. The material composition is given in Table 1. These specimens were spun in stages using wooden mandrels and thus there was not much variation in thickness along the meridian. The specimen details are given in Table 2, wherein the thickness is the mean of measurements at seven locations equally spaced between apex and base of the specimen. Typical variation of specimen thickness is given in Table 3. These specimens were subjected to impact loading between rigid flat platens in a drop mass setup shown in Fig. 1a. Impact tests were conducted with velocities ranging from 2 to 10 m/s and with a drop mass of 27 or 37 kg, as given in Table 4

The load was measured with the help of three Kistler load cells of capacity 30 Ton each as shown in Fig. 1b, forming an equilateral triangle. Output in voltage versus time was obtained through a Charge amplifier and



Fig. 1b. Drop mass setup – load cell arrangement.

recorded in a digital storage oscilloscope (Agilent 54624A). A scale factor of $1 \text{ mV} = 0.09 \text{ kN}$ determined from calibration charts was used to convert this to load–time response.

The velocity of the drop hammer just before the impact was measured by using two diodes for transmitting and receiving the infra red light. When the infrared light is obstructed by a strip of known width attached at the bottom of the drop mass, a signal displayed on the oscilloscope shows a voltage drop which gives the time period over which the light was obstructed. The initial impact velocity of the mass was obtained from this time period and width of the strip.

Quasi-static experiments were also performed on the above shells in a MTS universal testing machine at a crosshead movement of 2 mm/min .

Three distinct modes of collapse, namely local flattening, inward dimpling and formation of lobes were observed in different specimens subjected to both static and impact loading. Typical histories of deformation, load–compression curves, mean collapse loads, number of lobes formed, characteristic dimensions and the

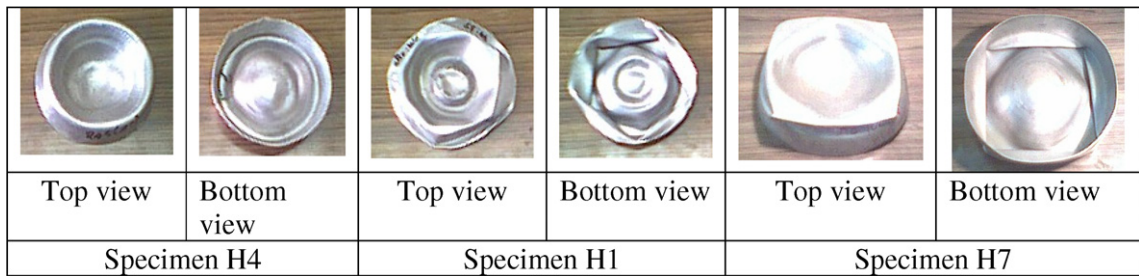


Fig. 2. Typical experimentally deformed profiles of hemi spherical shells.

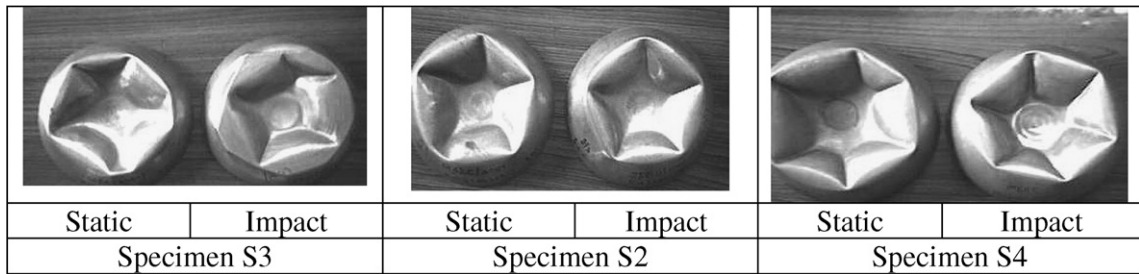


Fig. 3a. Typical experimentally deformed profiles of shallow spherical shells.

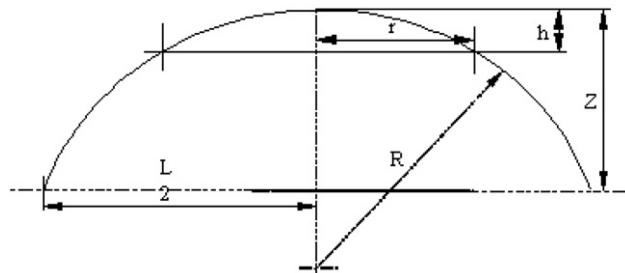


Fig. 3b. Schematic diagram showing the parameters (before deformation).

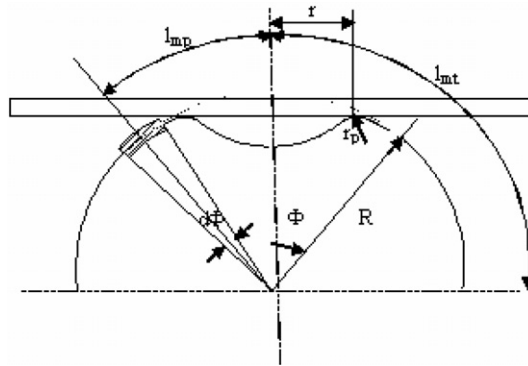


Fig. 3c. Schematic diagram showing the parameters (after deformation).

Table 5
Static and impact characteristic dimensions of deformed spherical shells

Spec. no.	R/t	Depth of deformation (mm)	Radius of parallel circle		Depth of inward dimple(mm)	
			Static	Impact	Static	Impact
H1	64.29	10.2	28.4	25.3	7.6	6.8
H2	50.00	14.6	33.1	30.1	10.5	9.4
H3	38.14	18.4	36.3	32.6	14.2	12.8
H4	28.13	22.6	38.8	34.5	16.4	14.2
H5	156.92	25.2	67.1	61.1	18.5	15.6
H6	114.6	30.6	72.8	65.5	24.6	21.6
H7	87.18	40.4	81.3	73.9	34.6	31.2
H8	218.57	58.2	119.8	110.1	46.2	38.9
H9	170.00	69.6	127.8	112.4	42.9	35.2
H10	129.66	75.6	131.6	125.4	58.6	46.3
S1	145.71	25.6	66.8	64.2	16.3	11.8
S2	114.61	32.2	72.2	70.1	21.5	18.2
S3	86.44	41.4	80.9	67.9	29.8	25.4
S4	218.57	35.2	97.3	90.4	26.1	21.3
S5	173.86	43.2	106.3	91.5	31.5	28.3
S6	129.16	51.4	114.4	105.3	39.4	32.4

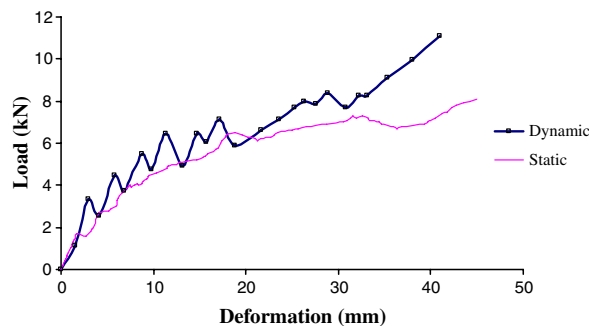


Fig. 4a. Typical experimental load–deformation curves for specimen S5.

deformed shapes at different stages of compression were obtained from these experiments and are presented. Influences of radius and thickness values of the shells on their energy absorption capacities are discussed. Results obtained in quasi-static tests were compared with the corresponding impact test results.

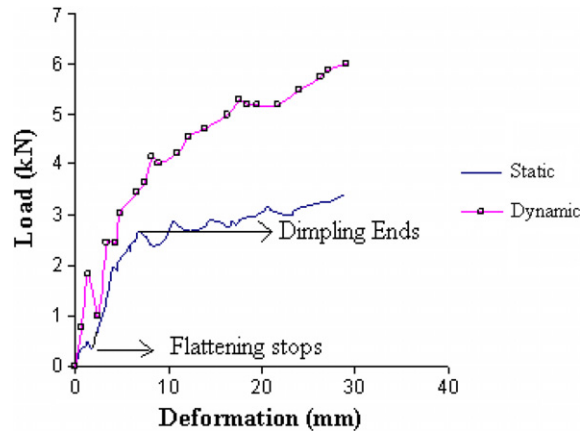


Fig. 4b. Typical experimental load–deformation curves for specimen S2.

3. Experimental results and discussion

It is seen from the present experiments that the spherical shells of thickness 1.6 mm, deformed mainly by the formation of a symmetric inward dimple. In all the shells of thickness equal to or less than 1.2 mm, however, the inward dimpling was followed by the formation of non-symmetric integral numbers of lobes. Top and bottom views of typical deformed hemi spherical specimens H1, H4 and H7, under impact loading, are shown in Fig. 2. For typical shallow spherical specimens S2, S3 and S4, deformed profiles obtained in impact experiments are compared with those obtained in static experiments in Fig. 3a.

For the given axial compression, the depth of inward dimple and the radius of parallel circle at the contact between the flat platen and the specimen, shown schematically in Figs. 3b and 3c, were recorded in both impact and quasi-static experiments and are given for comparison in Table 5. It was observed that values of the radius of parallel circle (r) and the depth of inward dimple were lesser in impact experiments than their corresponding values in static experiments.

For shallow spherical specimen S5 ($R/t = 173.86$ and $t = 0.9$ mm) and specimen S2 ($R/t = 114.61$ and $t = 0.9$ mm) load–deformation curves obtained in impact tests are shown in Figs. 4a and 4b. Corresponding static load–compression curves are also shown in these figures for comparison. To make the understating easier, stage-wise progress of the lobe formation for specimens H1 and H12 are shown in Figs. 4c and 4d. Load–deformation curves for specimens H11 and H12 are shown in Figs. 4e and 4f.

For all the impact tested specimens the load values were recorded using a 4-channel digital storage oscilloscope (Agilent 54624A). By cross-plotting the values of load versus time and deformation versus time, load–deformation curves were obtained. Integrating the area under the load–deformation curves we obtain the energy absorbed; the values thus obtained are given in Table 4. For computing the total compression of the specimen from the load–time curve of the shell, it is assumed that the drop mass is in continuous contact with the specimen during impact and its net displacement is equal to the compression of the specimen.

It was observed from the experimental data that the mean collapse loads obtained from the impact tests were always higher than those obtained from static tests by 10–20%. It was also observed that both the thickness and radius of the shells influence the mean collapse load. The variations of average load for various thicknesses of shells of 45 mm and 153 mm radii are shown in Fig. 5a. It was found that for shells of 1.2 mm thickness, if the radius is increased from 45 mm to 102 mm (2.3 times), the average load value is increased from 3.5 to 13.4 kN (3.8 times). Similar load variations with radii for the shells of thickness varying as 0.7, 0.9, 1.2 and 1.6 mm, are shown in Fig. 5b. It is noticed that for a radius of 102 mm, if the thickness is increased from 0.7 to 1.6 mm (2.3 times), the average load value is increased from 6.71 to 8.27 kN (1.23 times). Thus the influence of the shell thickness on the average load and the energy absorption is less pronounced than that of its radius.

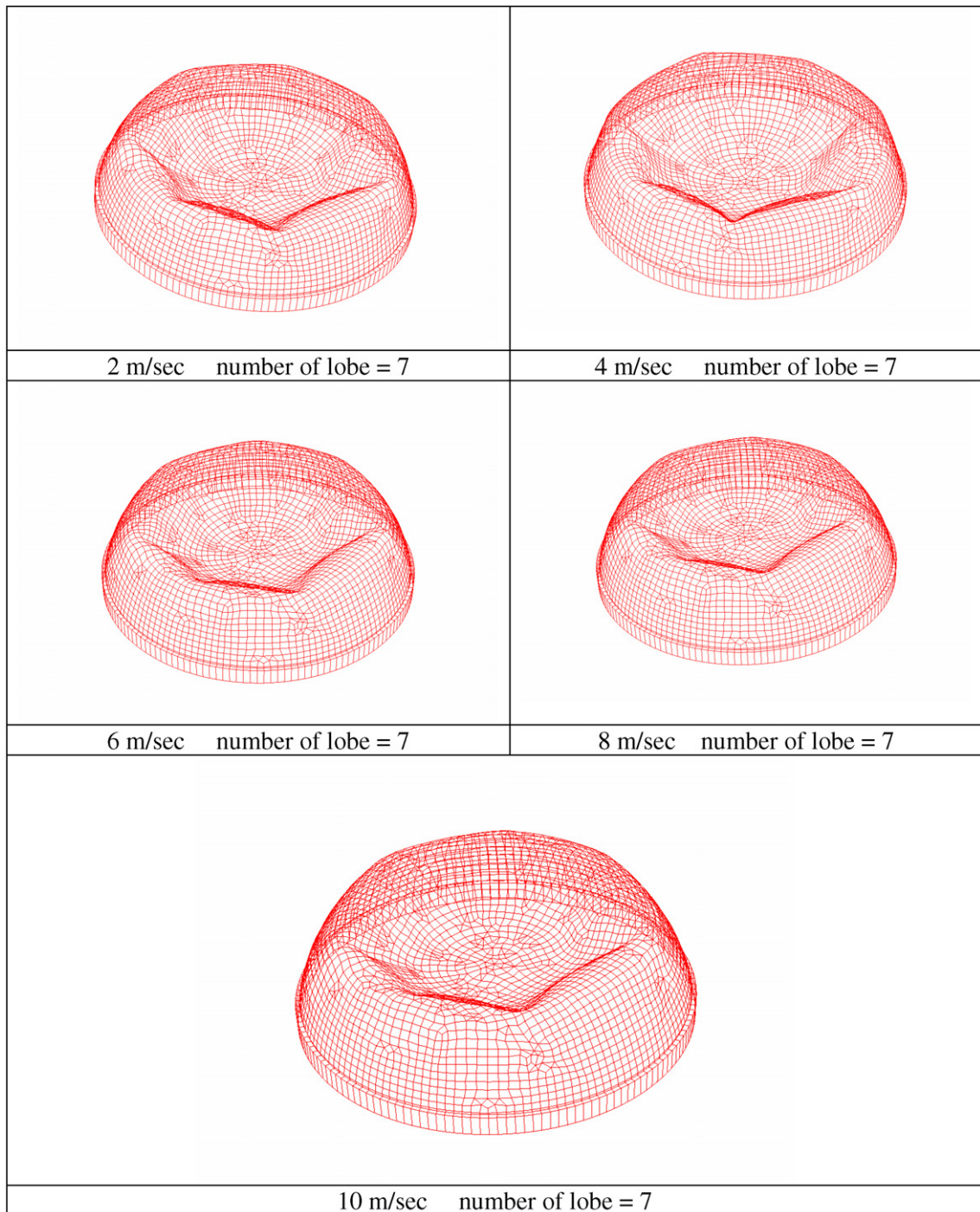


Fig. 4c. Progress of lobe formation with increase in velocity for specimen H1 (at various time steps).

The load–deformation curves obtained for the shells tested under impact loading have been shown in Fig. 6a for shallow spheres and Fig. 6b for hemi spheres. Comparing the energy absorption under dynamic conditions for shells of various thicknesses, it was observed that the shells of higher thickness absorb more energy, however, for shells of 0.9 mm and 1.2 mm thicknesses it was seen that this effect is predominant in

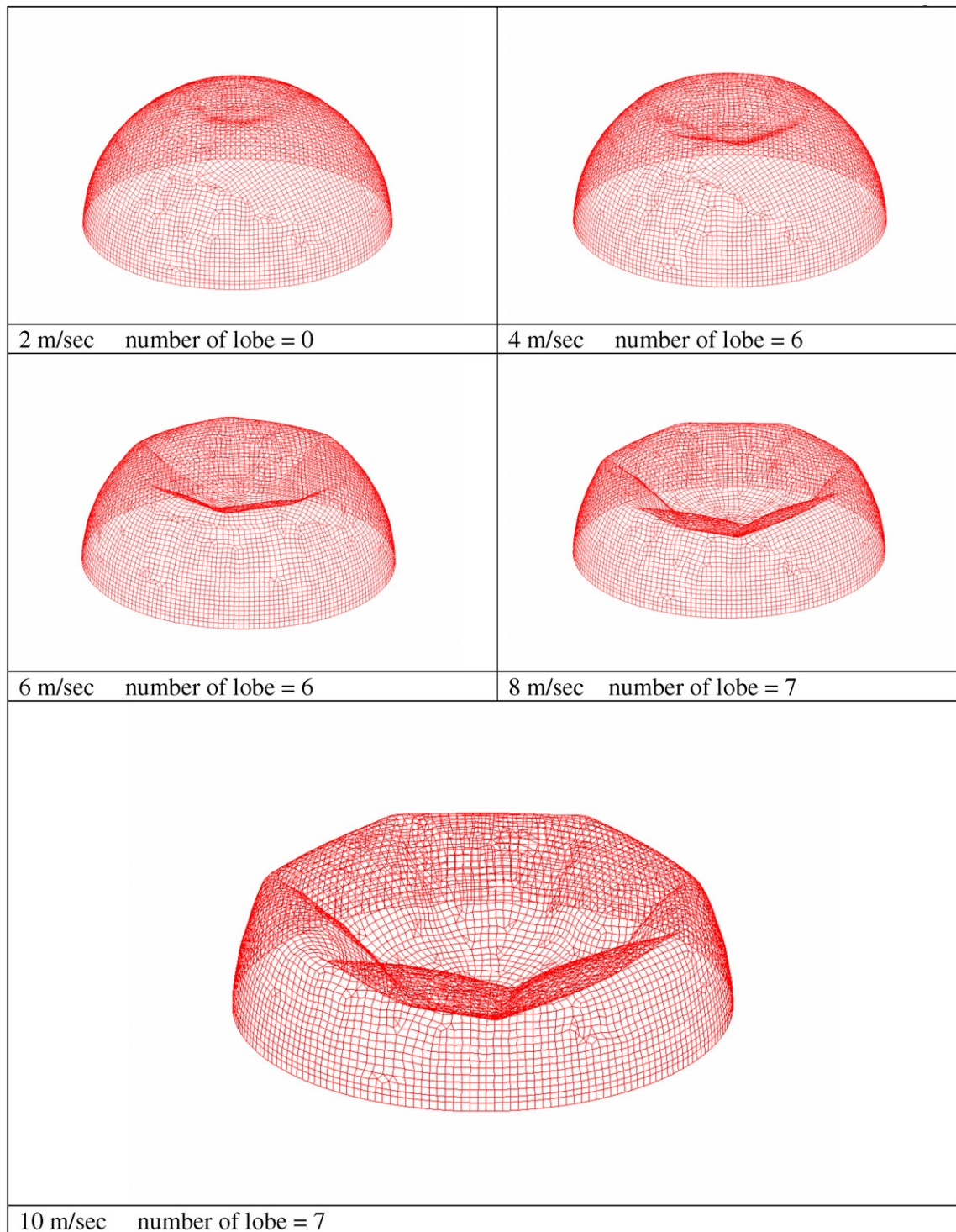


Fig. 4d. Progress of lobe formation with increase in velocity for specimen H12.

hemi spheres and moderate in the case of shallow spheres. This is because of the contribution of higher membrane strain in hemi spheres. Energy absorbed by various shallow spherical specimens under static loading is shown in Fig. 7 for comparison with the energy values presented for impact experiments in Fig. 6. The energy

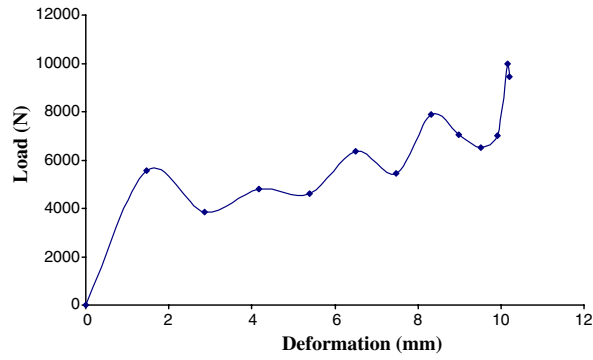


Fig. 4e. Load–deformation curve for specimen H11 at 2 m/s impact.

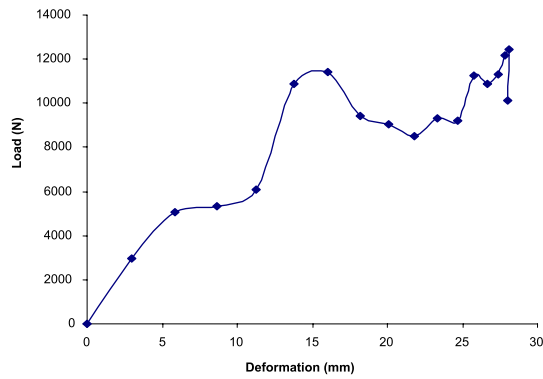


Fig. 4f. Load–deformation curve for specimen H12 at 4 m/s impact.

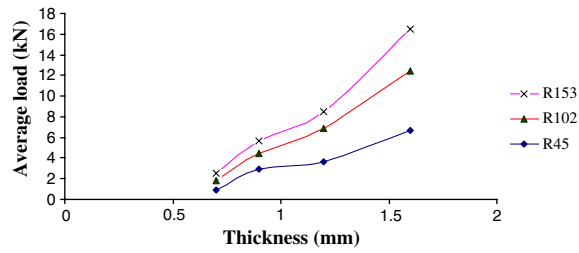


Fig. 5a. Variation of average load with thickness for various shell radii.

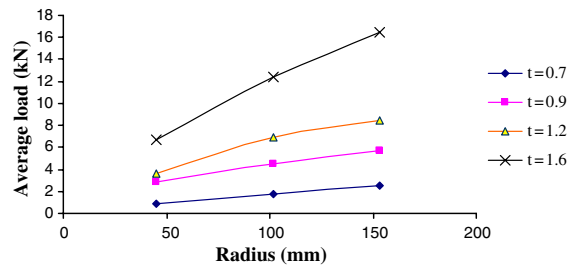


Fig. 5b. Variation of average load with radius for various shell thicknesses.

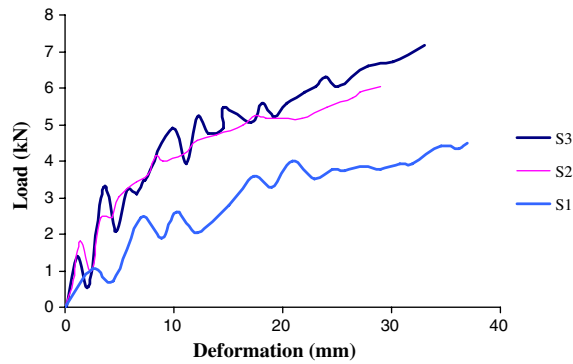


Fig. 6a. Impact Load–deformation comparison of various thicknesses of shallow spheres (specimen S1, S2, S3).

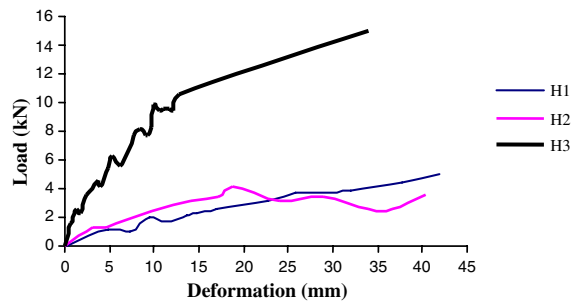


Fig. 6b. Impact load–deformation comparison of various thicknesses of hemi spheres (specimen H1, H2, H3).

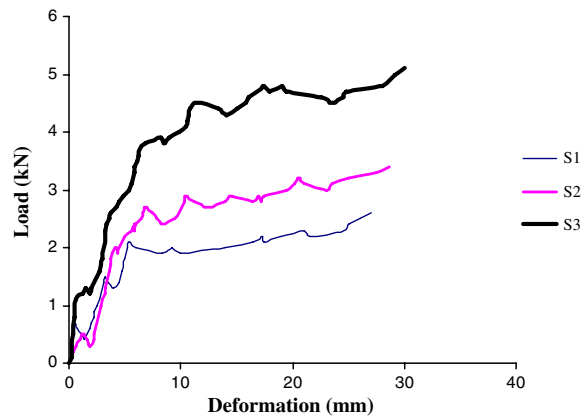


Fig. 7. Load–deformation curves for static experiments specimens S1, S2, S3.

absorbed in impact and static experiments is compared in the bar chart in Fig. 8, showing that the percentage increase in energy for hemi spherical shells compared to shallow ones is 18–33.

4. Numerical simulation

Collapse behaviour of the spherical shells under impact loading was numerically simulated using LS-DYNA[®]. The material and geometrical nonlinearities were incorporated in the analysis and the analysis was carried out by imposing the boundary conditions, which actually existed during impact tests. For

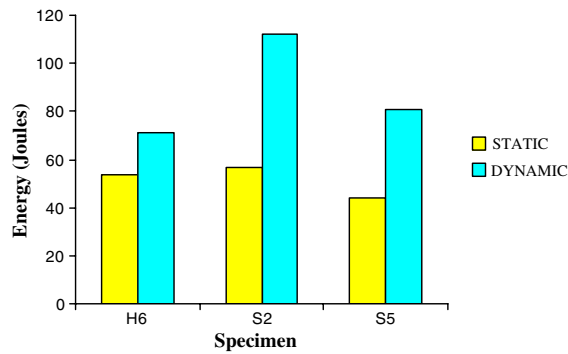


Fig. 8. Comparison of energy absorbed values obtained in impact at 2 m/s and quasi-static tests.

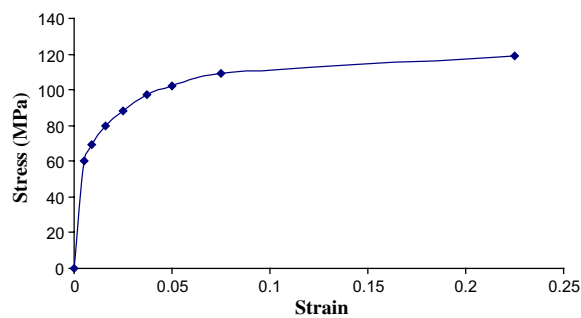


Fig. 9. Experimental stress–strain curve with the piecewise linearity points.

modeling, 4 nodes quadratic shell elements with three integration points were assigned to the specimen and rigid shell elements were used for the top and bottom plates. At the lower end of the specimen all degrees of freedom were arrested except the rotation about the axis of loading. The contact between the rigid plate and specimen was modeled using the option “nodes to impacting surface” with a friction coefficient of 0.1 to avoid lateral movements. Computations by varying the coefficient of friction from 0.08 to 0.12 showed that the load values varied by less than 0.5%. To account for the contact between the lobes, which was expected during the buckling of shells, a single surface contact algorithm without friction was used. Further, several trials were carried out to determine the proper mesh density for convergence.

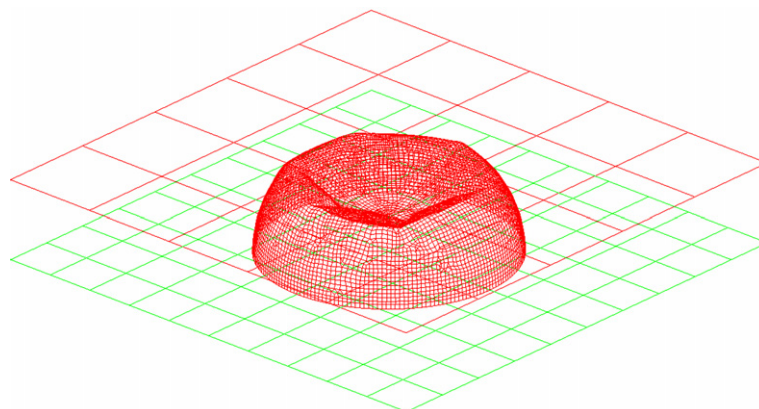


Fig. 10. Finite element model of specimen H5.

Experiments showed that the collapse modes of the shells were not symmetric throughout. Therefore in the present study full specimen was modeled as problem domain in an attempt to simulate all successive modes of deformation including the non-symmetric deformation. The X – Y plane was in the equatorial plane and the axis of the load coincided with the Z -direction (axis of rotation). The top platen was modeled to move on its axis with a downward velocity due to free fall of the hammer of given mass from a height (H), while the bottom plate was stationary. The Top platen was then allowed to fall from different heights in different simulations to give an impact velocity between 2 m/s and 10 m/s. Analyses were performed with a time step of 1 millisecond. The shell material in the plastic range was modeled as “Piecewise Linear Isotropic”. The material nonlinearity was included using the actual stress–strain curve obtained from the experiments along with the piecewise linearity points in the plastic region (see Fig. 9). The yield stress value for the multi-linear plastic curve was 55 MPa and it had Young’s modulus of 70 GPa. Material model 24 from LS-DYNA was employed: this is based on the Cowper-Symonds model which relates the dynamic and static yield stress by the relation

$$\sigma_y = \beta[\sigma_0 + f_h(\epsilon_{\text{eff}}^p)] \quad (4.1)$$

$$f_h(\epsilon_{\text{eff}}^p) = E_p(\epsilon_{\text{eff}}^p) \quad (4.2)$$

$$E_p = (E_t E / E - E_t) \quad (4.3)$$

where E is the Young modulus in the elastic region and E_t is the incremental tangent modulus in the plastic region. When these equations were used in the analysis, the computations showed that the instantaneous yield stress values increased from 55 to 75.49 MPa, when the impact velocity was increased from 2 to 10 m/s.

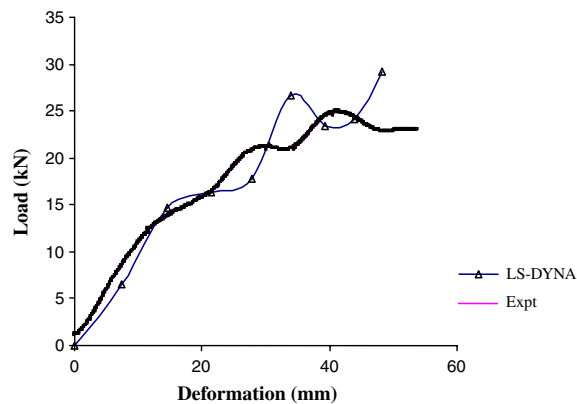


Fig. 11a. Comparison of impact experiment curve with LS-DYNA (at impact velocity of 10 m/s) – H4.

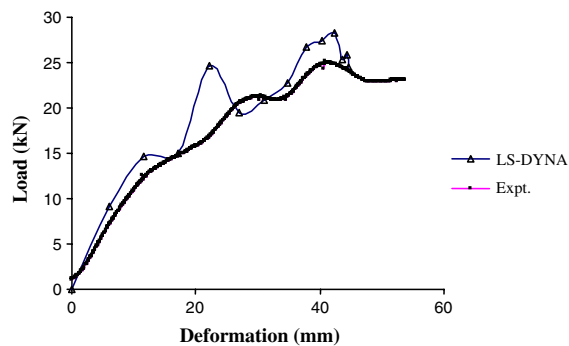


Fig. 11b. Comparison of impact experiment curve with LS-DYNA (8 m/s) – H4.

The contact between the impacting plate and the sample was specified as ‘automatic single surface title’. The boundary conditions of the bottom plate were completely arrested in order to simulate the rigid plate upon which the sample was placed during the impact test. Numerical simulations were carried out for all the specimens, up to the compression height for which the folds were formed.

Fig. 10 shows the numerical model of hemi spherical shell H5 and flat platens used for compression.

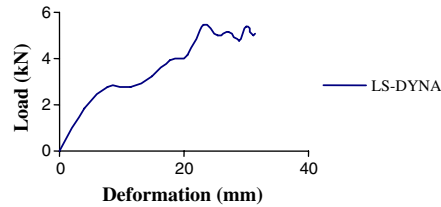


Fig. 12. Numerical – load–deformation curve for specimen H5 at velocity = 4 m/s (average load = 3.9648 kN, energy = 124.748 J).

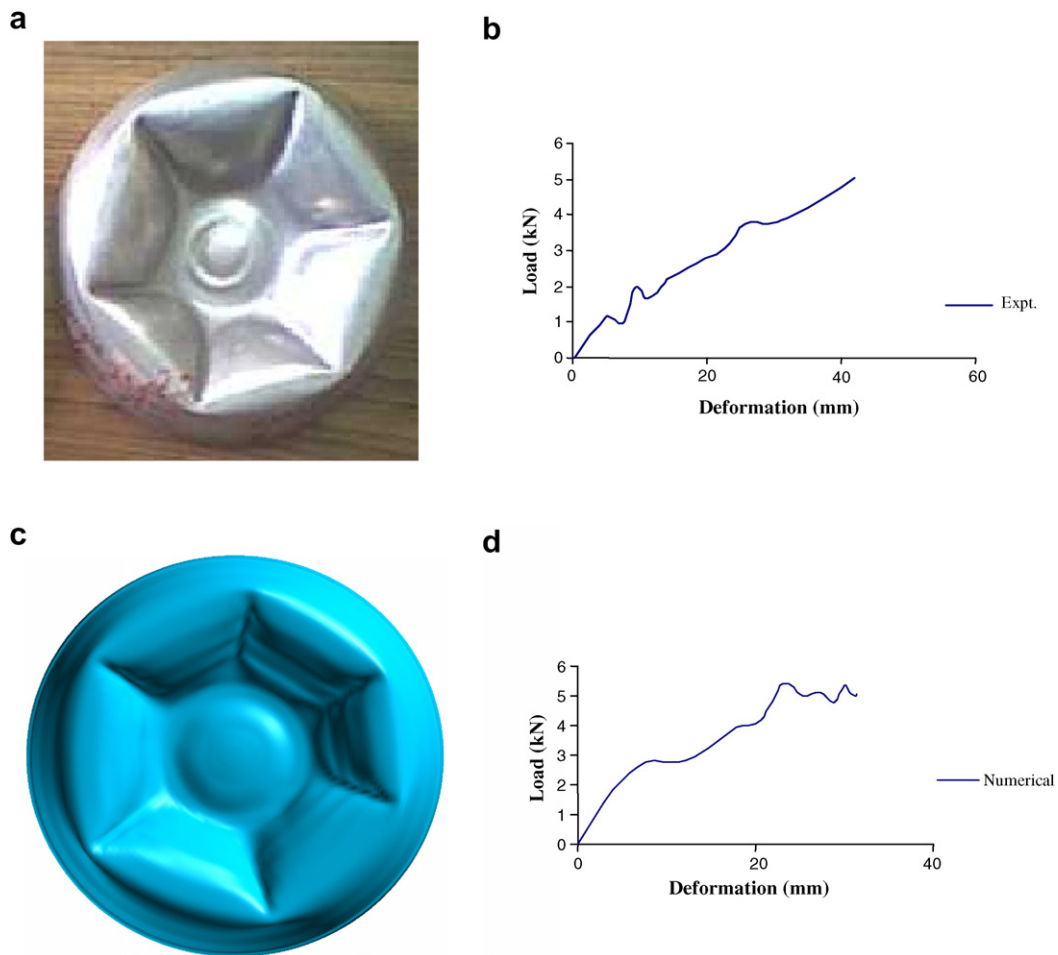


Fig. 13. Lobe comparison for hemi spherical samples under dynamic load: (a) impact experiment H5, (b) load vs deformation curve – experimental for H5, (c) numerical simulation – for specimen H5, (d) load vs deformation curve – experimental for H5.

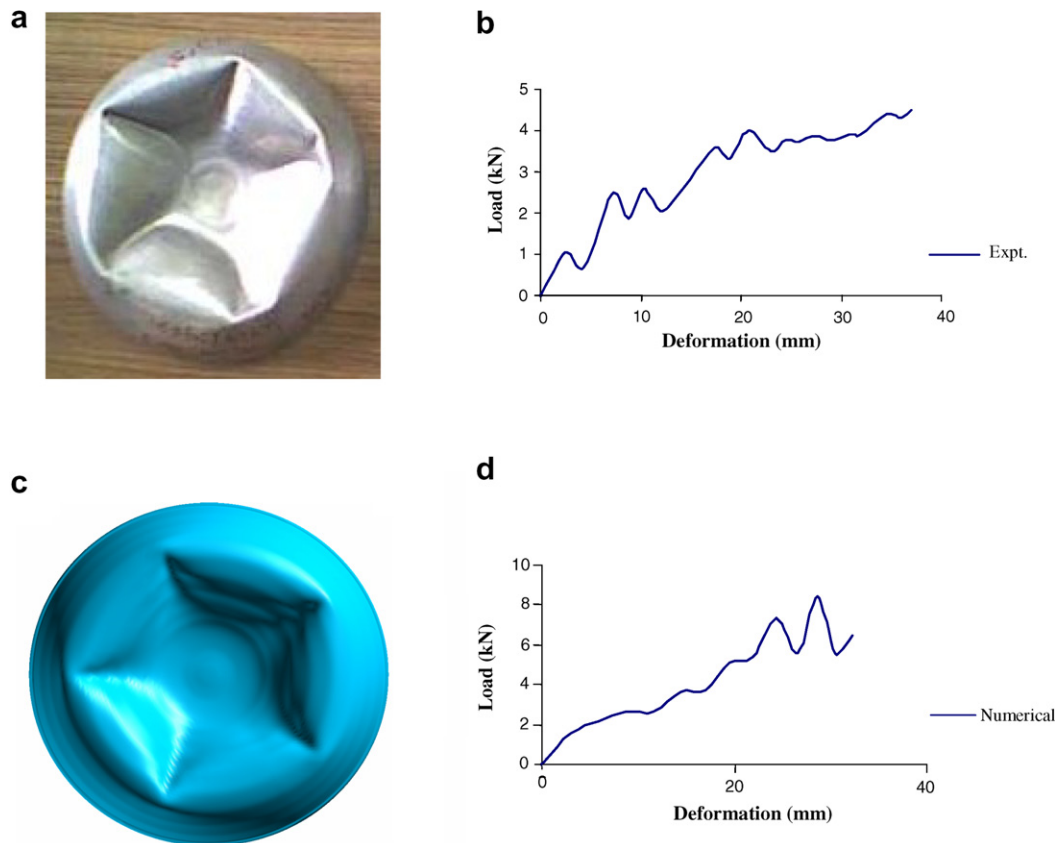


Fig. 14. Lobe comparison for shallow spherical samples under impact load: (a) impact experiment – S1, (b) load vs deformation curve – experiment for S1, (c) numerical simulation – for specimen S1, (d) load vs deformation curve obtained from simulation for S1.

5. Validation of numerical simulation

In the numerical simulation, hemi and shallow spherical specimens were compressed to the value equal to the maximum compression that occurred in the experiments (same velocity and drop height). Numerical model has been verified by comparing the experimental and numerical load–deformation curves. The deformed shapes of each specimen at different stages of compression were recorded. Typical load–deformation curves obtained from the numerical simulations at impact velocities of 8 m/s and 10 m/s are compared with the experimental curves in Figs. 11a and 11b.

Numerical analyses were carried out for various impact velocities. Typical results of the deformed shape of the hemi spherical shell (H5) impacted at 4 m/s is shown in Fig. 12.

Experimentally tested hemi spherical specimen H5 and its load–deformation curve are shown in Fig. 13a and b. Numerical simulation for buckling pattern and load–deformation curve are shown in Fig. 13c and d. It is noticed that the numerically simulated buckling pattern is in good agreement with the experimental results; both show six lobes. The load–deformation curve obtained in numerical simulation also shows similarity with the experimental curve with the average load of 3 kN as against the experimental value of 2.8 kN.

Experimentally tested shallow spherical specimen S1 and its load–deformation curve are shown in Fig. 14a and b. Numerical simulation for buckling pattern and load–deformation curves are shown in Fig. 14c and d. The load–deformation curve obtained in numerical simulation has an average load of 3.7 kN and the experimental average load is 3.2 kN.

For various hemi spherical specimens simulations were carried out at different velocities and parameters such as compression height, maximum peak load, mean collapse load and energy values were obtained and

Table 6
Numerical simulation-energy values for hemi spheres

Specimen	Comp. height in mm	Velocity in m/s	Max. load in kN	Average load in kN	Energy in J
H1	14.7	2	2.37	1.31	19.20
H1	23.2	4	3.30	2.24	51.97
H1	26.3	8	4.30	2.78	73.11
H1	32.1	10	4.98	3.25	104.33
H5	13.0	2	3.42	2.10	27.30
H5	31.5	4	5.42	3.97	124.75
H5	57.2	8	9.41	5.68	323.02
H5	61.1	10	12.02	5.39	329.20
H8	19.0	2	5.20	3.17	60.23
H8	44.3	4	5.93	3.99	176.70
H8	74.3	8	10.30	5.60	416.10
H8	76.4	10	15.15	6.65	507.80
H4	6.5	2	13.40	9.02	58.60
H4	16.4	4	24.20	14.60	224.80
H4	28.5	8	31.50	15.10	430.35
H4	32.0	10	42.70	19.83	634.60
Specimen with $R = 45$, $t = 1.4$	12.8	2	5.6	4.2	53.76
	16.3	4	8.2	6.8	110.84
	19.4	8	10.4	8.3	161.02
	22.1	10	14.2	12.1	266.20
Specimen with $R = 153$, $t = 2.0$	14.6	2	8.2	6.1	89.16
	27.3	4	10.4	8.1	221.13
	39.6	8	16.7	14.4	570.24
	48.8	10	20.6	17.3	844.24

Table 7
Numerical simulation – energy values for shallow spheres

Specimen	Comp. height in mm	Velocity in m/s	Max. load in kN	Average in kN	Energy in J
S1	17.4	2	7.10	3.49	60.65
S1	36.9	4	14.90	5.73	211.32
S1	48.8	8	28.10	6.26	305.49
S1	52.2	10	15.90	6.41	334.60
S3	19.0	2	5.77	3.15	59.90
S3	42.0	4	8.22	4.89	205.38
S3	77.2	8	14.66	6.14	474.01
S3	82.4	10	16.62	7.12	586.69
Specimen with $R = 102$, $Z = 72$ and $t = 1.4$	18.2	2	4.30	3.90	70.98
	37.6	4	6.70	5.20	195.52
	51.8	8	8.20	7.30	378.14
	63.3	10	13.20	11.40	721.62
Specimen with $R = 153$, $Z = 102$ and $t = 2.0$	7.1	2	9.20	7.20	51.12
	21.5	4	11.60	9.60	206.40
	49.3	8	16.40	14.40	709.92
	63.6	10	22.20	18.80	1195.68

are given in Table 6. Similarly for shallow spherical specimens the details are given in Table 7. These Tables include numerical simulation for specimens of thicknesses 1.4 and 2 mm. for which we had no experimental results.

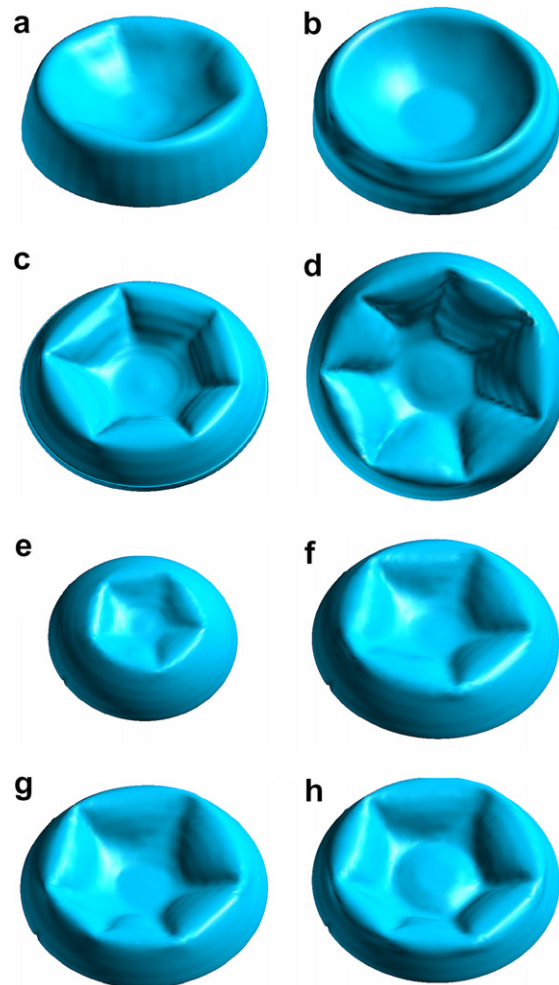


Fig. 15. Numerical simulation for number of lobes: (a) H5 at 2 m/s, (b) H5 at 4 m/s, (c) H5 at 6 m/s, (d) H5 at 10 m/s, (e) S4 at 2 m/s, (f) S4 at 4 m/s, (g) S4 at 8 m/s, (h) S4 at 10 m/s.

6. Discussion on results

The three-dimensional finite element analysis presented is of help in predicting all the stages of collapse of the spherical shells under impact loading. The geometry of the deformed shell at each time step was obtained from the post processor LS-POST of the software. The results of the deformed geometry match with the experiments well, including various modes of collapse, their transitions and number of non-axisymmetric folds formed.

Out of all the geometries considered in the present analysis, the formation of non-axisymmetric folds was observed in the shells of thickness varying between 0.7 mm and 1.2 mm both experimentally and numerically. The numerical results obtained for various specimens at different velocities are shown in Fig. 15a–h. It was observed that the number of lobes formed varied between 5 and 7.

The experimentally obtained deformation patterns are compared with those obtained from numerical simulation and are shown in Fig. 16a–h. It is observed that the numerical results match well with the experiments both in terms of number of lobes as well as their geometry.

Having validated the numerical procedure with experimental data, the variation of the load and the energy absorption with impact velocity were numerically determined for the shells of different thicknesses. For veloc-

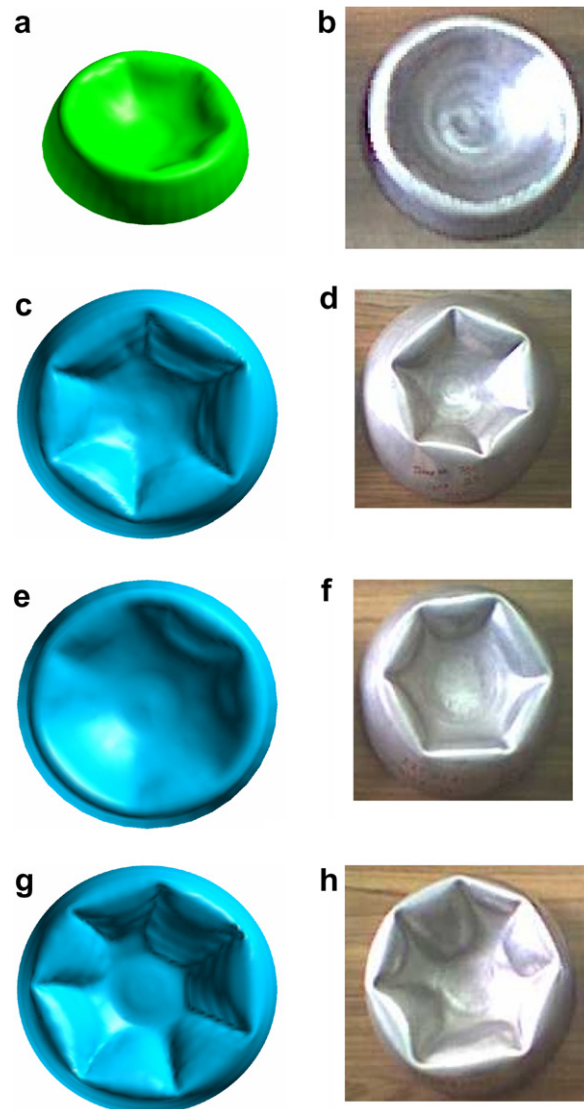


Fig. 16. Comparison of numerical and experimental lobe formation: (a) H5 at 4 m/s (numerical), (b) H5 at 4 m/s (experimental), (c) H10 at 10 m/s (numerical), (d) H10 at 10 m/s (experimental), (e) H7 at 4 m/s (numerical), (f) H7 at 4 m/s (experimental), (g) H8 at 8 m/s (numerical), (h) H8 at 8 m/s (experimental).

ities ranging between 2 and 10 m/s, the numerically obtained variation of average load is shown in Fig. 17a for hemi spherical shells of thickness 1.6 mm. The corresponding energy values are shown in Fig. 17b.

Variation of the numerically obtained average load with the impact velocity for shallow spherical shells with thickness 0.7 mm is shown in Fig. 17c, and the corresponding energy values are shown in Fig. 17d. It is observed that the average load increases as the velocity increases. In Fig. 18, a comparison has been made for the experimentally obtained average load values with the numerical results for various impact velocities.

7. Conclusions

The collapse behaviour of aluminium hemi and shallow spherical shells of different radius to thickness ratios were investigated experimentally and numerically. The computed load–deformation curves at different stages of compression are found to match well with those obtained from experiments. The predicted deformed

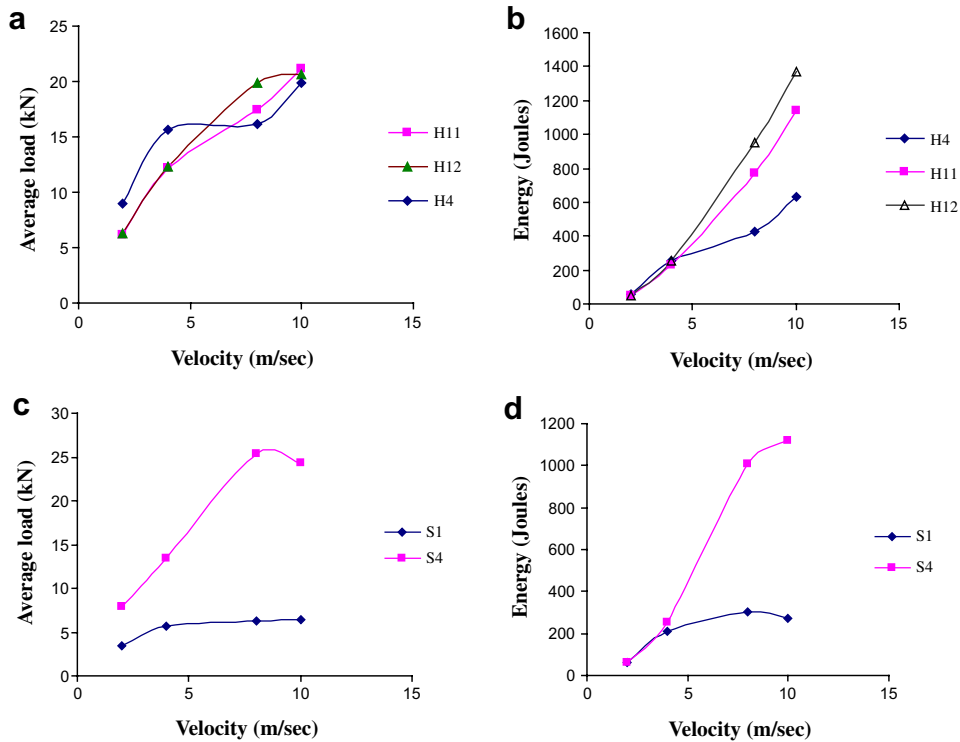


Fig. 17. Variation of parameters against velocity for different hemi spherical specimens: (a) velocity with average load and (b) velocity with energy. Variation of parameters against velocity for different shallow spherical specimens: (c) velocity with average load and (d) velocity with energy.

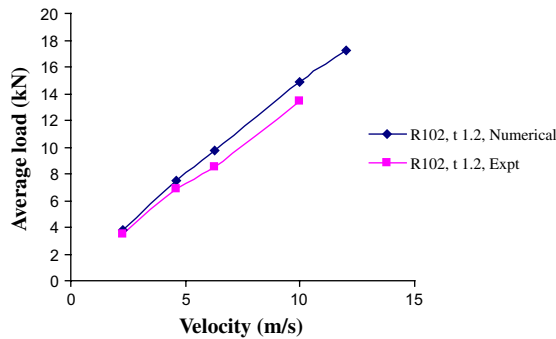


Fig. 18. Comparison of Numerical and experimental average load values (H7).

shapes at different stages of compression viz, local flattening, inward dimpling and formation of non-axisymmetric lobes are also found to be in good agreement with the actual deformed profiles. It is seen that as the R/t value increases, the range of compression over which the elastic deformations occur decreases. The number of lobes varied between 5 and 7 depending upon the R/t values. Out of the geometries chosen for the present study, experiments showed that the shells of thickness 1.6 mm deformed mainly in axi-symmetric mode, resulting in the formation of inward dimple.

The impact mean collapse load and hence the energy absorbed during deformation are found to be higher than their corresponding static values, and are found to be dependent on both thickness and radius of the shell.

References

- De'Oliveria, J.G., Wierzbicki, T., 1982. Crushing analysis of rotationally symmetric plastic shells. *J. Strain Anal.* 17, 229–236.
- Gupta, N.K., Venkatesh, 2004. Experimental and numerical studies of dynamic axial compression of thin walled spherical shells. *Int. J. Impact Eng.* 30, 1225–1240.
- Gupta, N.K., Eswara Prasad, G.L., Gupta, S.K., 1999. Axial compression of metallic spherical shells between rigid plates. *Thin Walled Struct.* 34, 21–41.
- Kinthead, A.N., Jennings, A., Newell, J., Leinster, J.C., 1994. Spherical shells in inelastic collision with a rigid wall tentative analysis and recent quasi-static testing. *J. Strain Anal.* 29, 17–41.
- Kitching, R., Houston, R., Johnson, W., 1975. A theoretical and experimental study of hemi spherical shells subjected to axial loads between flat plates. *Int. J. Mech. Sci.* 17, 693–703.
- Udike, D.P., 1972. On the large deformation of a rigid plastic spherical shell compressed by a rigid plate. *J. Eng. Ind.*, 949–955.